

Reaching high flux in laser-driven ion acceleration^{*}

Felix Mackenroth^{1,2,a}, Arkady Gonoskov^{2,3,4}, and Mattias Marklund²

¹ Max Planck Institute for the Physics of Complex Systems, Nöthnitzer Str. 38, 01187 Dresden, Germany

² Department of Physics, Chalmers University of Technology, 41296 Göteborg, Sweden

³ Institute of Applied Physics, Russian Academy of Sciences, 603950 Nizhny Novgorod, Russia

⁴ Lobachevsky State University of Nizhni Novgorod, 603950 Nizhny Novgorod, Russia

Received 16 March 2017 / Received in final form 17 May 2017

Published online 3 August 2017

© The Author(s) 2017. This article is published with open access at Springerlink.com

Abstract. Since the first experimental observation of laser-driven ion acceleration, optimizing the ion beams' characteristics aiming at levels enabling various key applications has been the primary challenge driving technological and theoretical studies. However, most of the proposed acceleration mechanisms and strategies identified as promising, are focused on providing ever higher ion energies. On the other hand, the ions' energy is only one of several parameters characterizing the beams' aptness for any desired application. For example, the usefulness of laser-based ion sources for medical applications such as the renowned hadron therapy, and potentially many more, can also crucially depend on the number of accelerated ions or their flux at a required level of ion energies. In this work, as an example of an up to now widely disregarded beam characteristic, we use theoretical models and numerical simulations to systematically examine and compare the existing proposals for laser-based ion acceleration in their ability to provide high ion fluxes at varying ion energy levels.

1 Introduction

Producing beams of high-energy ions by compact, laser-based accelerators for numerous applications ranging from material and energy science [1] to even medical applications [2] has received considerable interest and effort over the past decade [3,4]. The principal work horse of laser ion-acceleration up to now is the robust and widely studied scheme of target normal sheath acceleration (TNSA) [5–10]. This scheme, however, suffers from a number of severe drawbacks [11], including (i) a disfavorable scaling of achievable ion energies with increasing laser intensity [12], limiting the scheme's efficiency at higher laser intensities, (ii) a limited control over the acceleration, as is apparent from the mostly thermal ion energy spectrum, hindering the precise tuning of the target ion energies, as well as (iii) a low efficiency of the acceleration mechanism at high laser powers [13]. Many of these drawbacks, however, can be counteracted to some extent by specially designed targets [14–17] and laser pulse shapes [18,19]. Thus, the comparatively simple design and operation of TNSA accelerators renders it a promising mechanism for the construction of reliable and stable lower-energy laser ion-accelerators. On the other hand, in order to compensate for the mentioned drawbacks, there

have been a number of novel ion acceleration schemes proposed. Among the standard of these novel acceleration schemes is, e.g., Coulomb explosion (CE) of clusters [20–22] and double-layered targets [23–26], designed to provide narrow energy spreads for the generated ion beams. Next to these schemes, which still rely on an expanding electron cloud due to local plasma heating, new schemes were introduced promising a more direct energy transfer from the laser pulse to an accelerated ion bunch, such as collisionless shock acceleration [27,28], hole boring (HB) [29] or laser piston, also referred to as light sail (LS) [30–34], or entirely new approaches [35]. Hole boring and light sail acceleration schemes aim at directly employing the laser's light pressure to move the plasma electrons, which subsequently pull the heavier ions by the Coulomb field, thus promising a more controllable energy transfer and hence more easily tunable ion bunch properties as well as a higher efficiency. All the above mentioned laser ion-acceleration schemes are predicted to surpass the capabilities of TNSA by aiming at higher laser intensities and powers, as will become available in the coming years¹ [36], whence one can subsume them under the general term *high-power schemes*. At this point it is important to note, on the other hand, that there exist several specific applications requiring dense ion beams of comparatively low particle energies, such as warm dense matter production or neutron sources. For these it might be favorable to operate

^{*} Contribution to the Topical Issue “Relativistic Laser Plasma Interactions”, edited by Tünde Fülöp, Francesco Pegoraro, Vladimir Tikhonchuk.

^a e-mail: mafelix@pks.mpg.de

¹ ELI, <http://www.extreme-light-infrastructure.eu/>; XCELS, <http://www.xcels.iapras.ru/>.

the laser-acceleration schemes, labeled *high-power* previously, already at low laser powers, to generate precisely this kind of ion beams. Such applications, however, are not within the scope of this work.

The concept of TNSA has been well studied in experiment [5,7,8] and is supported by a well developed theory [6,37–41] based on earlier studies of the expansion of heated plasmas into vacuum [42–46]. Assessing the prospects of the mentioned high-power acceleration mechanisms is a still ongoing and demanding effort in both experiment and theory. Despite the analytical models developed for each mechanism, several issues make it difficult to directly compare their potentials in accelerating ions. Firstly, each mechanism requires adjusting the parameters of the target, which can depend also on the laser pulse's parameters, such as total energy, duration, focal spot size or pulse contrast. Secondly, not only the peak or average energy, but also many other characteristics of the produced ions may be of crucial importance for certain potential applications. For instance, some schemes may provide higher ion energies, sacrificing the total number of accelerated particles, possibly even reducing the overall energy of the accelerated ion bunch. Apart from high ion energies, however, potential applications of laser-based ion sources pose requirements on such other characteristics of the ion beams as, e.g., the number of ions accelerated to a certain required energy level, the directionality of these ions and the repeatability of the generation process. Determining the most promising strategies and their capabilities in terms of above-mentioned characteristics can play a key role for identifying the applications that can most beneficially be realized with compact laser-based ion sources.

In this work we present a systematic study of the most common high-power laser ion-acceleration schemes in terms of their ability to provide high flux of ions for several particular levels of energy. This parameter, as formally introduced below, is a single parameter measuring the overall energy content of the ion beam, hence offers a way of comparing the performance of various acceleration schemes to transfer a given amount of laser energy, usually preset by the experimental facility operating the laser-ion accelerator, into kinetic energy of accelerated ions. Furthermore, the total energy content of the accelerated ion beam, i.e., its flux, has direct meaning several important applications such as, e.g., medical hadron therapy, where the ion flux determines the total dose the accelerator can possibly deliver. One drawback of such a single-parameter approach naturally is the impossibility of distinguishing whether the ion beam stores its energy in many low energy particles or just a few particles with high energies. Such a multi-parametric study, however, is beyond the scope of providing a clear benchmarking, as pursued in this work.

Apart from TNSA, in this study we consider three of the alternative schemes mentioned above, namely Coulomb explosion, hole boring and light sail, since they exemplify the fundamentally different physical processes and main driving mechanisms for laser-based acceleration schemes in solid targets. We assess the schemes' prospects using particle-in-cell (PIC) simulations and previously developed analytical models. Since the analytical models

are based on a one-dimensional geometry, two-dimensional simulations, as presented here, already provide a good insight into the way the physics can deviate from the assumed one-dimensional scenarios. To study these acceleration schemes we keep the laser parameters fixed and consider four classes of target designs, optimized for the various schemes (s. Fig. 1). Such optimizations are customarily assumed for various high-power schemes regarding, e.g., the target thickness [47]. This practice is motivated by striving to provide the most valuable information for laser facilities where the laser parameters are largely fixed but the target may be changed. For full comparability we analytically, as well as numerically, benchmark the results of the high-intensity schemes against TNSA, simulating a target optimized for TNSA as well. Finally, to provide a concise comparison of the studied laser acceleration schemes in terms of only one parameter, we use an ion momentum flux density as a basic efficiency measure applicable to different acceleration schemes.

The paper is organized as follows: after the introduction we provide a concise definition and discussion of the relativistic ion current, employed as the single parameter quantifying the laser-ion acceleration schemes' efficiency, employed laser parameters, the configuration of the performed simulations and an estimate of thermal noise level. Next, we summarize the known analytical theories and compare the theoretical predictions to a performance analysis in a two-dimensional PIC simulations for the three high-power acceleration schemes Coulomb explosion, hole boring and light sail. Finally, we compare all schemes to each other and benchmark their respective performance against TNSA.

2 Analytical models and 2D PIC simulations

2.1 Relativistic ion current

A possibly problematic issue in comparing the various different high-intensity ion acceleration schemes is that they have all been optimized and benchmarked with the emphasis put on different aspects of possible applications of high-energy ion beams. Thus, in each optimization different benchmark parameters were employed, such as peak energies [31,48,49], number of accelerated particles [50] as well as a small width of the ion distribution in energy [26,28,51–53] or space [54]. In order to assess the performance and potential of the various ion acceleration schemes we are thus going to study a single parameter, in order to put all ion acceleration schemes in context. A suitable parameter for this task is the relativistic ion current, or flux of momentum, generated by the laser acceleration, defined as

$$\mathbb{J} = \int d^3r \gamma(\mathbf{r}) \frac{\mathbf{v}(\mathbf{r})}{c} n(\mathbf{r}), \quad (1)$$

where $\mathbf{r} = (x, y, z)$ is the spatial coordinate, $\mathbf{v}(\mathbf{r})$ is the ions' velocity, $n(\mathbf{r})$ the particle density, $\gamma(\mathbf{r}) = (1 - (\mathbf{v}(\mathbf{r})/c)^2)^{-1/2}$ the Lorentz factor and the division by the speed of light c turns the current into a dimensionless

measure quantifying the total number of accelerated ions weighed with their relativistic factor. For a homogeneous ion bunch of constant velocity the current obviously reduces to the product of the particle number and the relativistic factor $\gamma\mathbf{v}/c$, indicating that the current indeed is a good measure for the bunch's overall energy content. We thus employ this parameter to benchmark all the studied ion acceleration schemes' efficiency in transforming the input laser energy into output ion beam energy.

Since we are studying the acceleration schemes numerically in a two-dimensional geometry, however, we are going to study a two-dimensional equivalent of the ion current \mathbb{J} , labeled *ion current density* \mathbf{j} . This takes into account that the transverse dimension, not resolved in our simulations, is assumed to feature translational symmetry. Thus, instead of the volumetric integral over the particle density $n(\mathbf{r})$ in our study we only perform a two-dimensional areal integral over the two dimensions resolved in the simulations

$$\mathbf{j} = \int dx dy \gamma(\mathbf{r}) \frac{\mathbf{v}(\mathbf{r})}{c} n(\mathbf{r}), \quad (2)$$

where we have chosen the target normal to coincide with the x -axis and labeled the resolved perpendicular coordinate y . Since we only consider the accessible ion current, propagating along the target normal direction the decisive, one-dimensional measure to quantify the acceleration schemes is

$$j_x \equiv j = \int dx dy \gamma(\mathbf{r}) \frac{v_x(\mathbf{r})}{c} n(\mathbf{r}). \quad (3)$$

Whereas the three-dimensional current is dimensionless, as argued above, in the present case the ion current density is given per unit distance in the non-resolved perpendicular coordinate direction. As a typical length unit of the studied ion acceleration we will always give it in $[j] = \mu\text{m}^{-1}$. In order to recover a conventional, dimensionless three-dimensional current one can multiply the simulation results with an assumed perpendicular extent of the accelerated ion bunch. As a good approximation this extent can be assumed to be equal to the ion bunch's diameter, which is of order of the laser spot size.

2.2 Laser parameters

We aim at modeling laser parameters as are mostly available at present or upcoming high-power laser facilities. For the best comparability of various laser acceleration schemes we need to consider a generic laser system, without focusing on a specific machine. Consequently, we consider a laser pulse with specifications similar to what is most broadly available: we consider a central wavelength $\lambda_0 = 810$ nm (frequency $\omega_0 = 2\pi c/\lambda_0$), FWHM pulse duration $\tau_0 = 44$ fs, with a Gaussian profile focused to a FWHM beam waist radius $w_0 = 10$ μm . We only vary

the pulse's total peak power P_0 . Its peak intensity is consequently given by $I = 2P_0\sqrt{\log 2}/(w_0^2\sqrt{\pi})$. For the best performance of the mentioned high-power acceleration schemes we model the laser pulse to be circularly polarized and to hit the target under normal incidence, except in the simulation of TNSA, where a linearly polarized laser pulse hits the target at an incidence angle of $\pi/4$.

2.3 Target configuration

In order to systematically benchmark the analytical models, it is required to compare their predictions to numerical solutions of the relevant plasma equations. We made use of the PIC code PICADOR, details of which were elaborately presented in earlier work [55]. We performed two-dimensional simulations, since they capture the one- or two-dimensional nature of the involved mechanisms as well as the possible formation of instabilities. Also, the benchmarking of the analytical models, all formulated in a one-dimensional geometry, against a two-dimensional simulation will already unveil whether significant drawbacks of its applicability are found.

To the end of identifying differences between the acceleration schemes from simulations it is sufficient to model an idealized target, posing a compromise between targets optimized for all separate ion acceleration schemes. In doing so, we deliberately neglect all target optimization, which was envisaged to boost the schemes' performance, for the sake of a systematic comparability of their bare energy conversion efficiencies. Furthermore, we will neglect all changes in the target's ionization states due to changing laser power, in order to keep the simulations as close to the analytical models as possible. Thus, we model targets consisting of electrons, protons (mass m_p , charge $-e$) and heavy ions (mass $20m_p$, charge $-e$), corresponding, e.g., to a high ionization state of iron. As such an idealized target, for hole boring, light sail, and Coulomb explosion acceleration we model targets consisting entirely or in parts of a macroscopic layer composed exclusively of hydrogen. As such pure hydrogen targets are challenging to produce at solid densities, we simulate a low target density consistent with novel cryogenic solid hydrogen jet targets [56], which are expected to give major benefits for the operation of laser-proton accelerators and whose operation was already successfully demonstrated [57]. For TNSA, the modeled hydrogen layer on the backside of a low-density target consisting of heavy ions can be realized, e.g., by a natural water vapor contamination on the backside of a foam target [58], homogenized by ionization due to the laser's prepulse. To minimize the impact of differing target compositions on the comparability of the simulation results, we thus model targets with varying geometry but a number density, dictated by the most important parts of the targets, i.e., the macroscopic hydrogen layer, of $n_0 = 30n_{\text{cr}}$ with the critical density $n_{\text{cr}} = m_e\omega_0^2/4\pi e^2$, where m_e ($e < 0$) is an electron's mass (charge). The thickness of the target will be chosen for each acceleration scheme

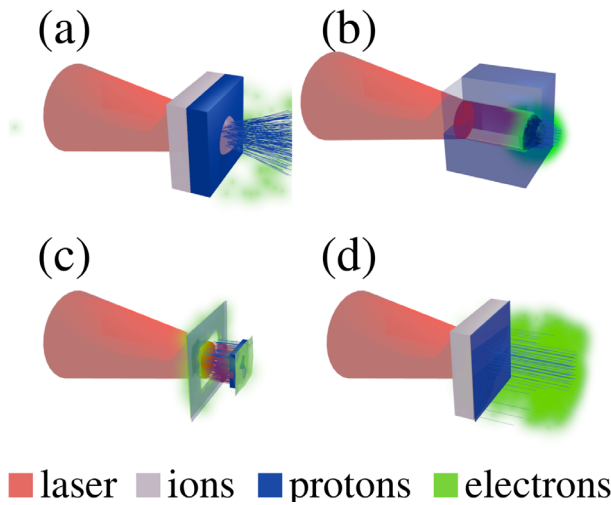


Fig. 1. Laser (from left in red) impinging on optimized target designs for the studied high-power ion acceleration schemes: (a) for the study of Coulomb explosion we model a double-layered target consisting of electrons (green), protons (blue) and heavier ions (light purple), (b) for hole boring we consider a thick proton target, (c) for a light-sail we study a thin layer of protons and electrons and (d) for the benchmarking TNSA we study a thick target of heavy ions with a thin proton layer on the back.

separately and is denoted by d_{LS} , d_{CE} , d_{HB} for the respective schemes. In all studied acceleration schemes the heavy ions serve as a mount for the lighter protons and are not significantly accelerated. We thus focus the present work on the current of accelerated protons. In extracting the current density from the simulations consequently only protons were counted, weighed with their momentum along the target's normal along the x -direction. Generalizing the results to other species of light ions is, however, straightforward.

While the analytical estimates are carried out irrespective of the specific target design, each of the calculations reviewed below assumes its underlying physical mechanism to work optimally. To ensure that this is indeed the case for each respective acceleration mechanism, one has to invoke certain, optimized targets. In order to fully assess the wide range of targets optimized for the various introduced high-power ion acceleration schemes we chose to perform numerical experiments on various different target geometries (s. Fig. 1).

In the numerical spectra we only account for protons with kinetic energies above a certain lower cutoff energy ε_{cut} , since experimentally there is only limited interest in the large abundance of low-energy, mostly thermal protons in the accelerated bunch. Furthermore, this exclusion reduces the impact of thermal noise that needs to be taken into account self-consistently in the simulations, as explained below. Thus, unless specifically mentioned, we employ a lower cutoff energy of $\varepsilon_{\text{cut}} = 5$ MeV. For assessing the contribution of high-energy protons to the current, however, we also provide spectra for lower cutoff energies of $\varepsilon_{\text{cut}} = 10$, $\varepsilon_{\text{cut}} = 50$ and $\varepsilon_{\text{cut}} = 75$ MeV.

2.4 Thermal noise

It is known that every solid target hit by a high-power laser is already heated by the laser's prepulse to a high temperature before the main pulse arrives. While it is also known that the prepulse has an abundance of further effects, such as thermal expansion of the target leading to an extended plasma corona [59], in this work we aim at a fundamental comparison of the studied models and choose to neglect such deeper intricacies. As only effect of the laser's prepulse we model the target to consist of ions and electrons in thermal motion. Such a finite initial plasma temperature is also unavoidable in numerical simulations, as a plasma artificially initialized with zero temperature would be numerically unstable. It is, as just argued however, not unphysical but related to the prepulse. To account for this pre-heating effect and to estimate the resulting numerical background for the simulated proton currents, we initialize the particles in our numerical experiments with an initial temperature T_0 . The corresponding random motion constitutes a current, due to thermal noise. To estimate the level of thermal noise, that could obscure the results of the simulations we estimate that each plasma particle in the simulation box has an initial thermal energy of $3k_B T_0/2$. Since we are only measuring the current in one spatial direction which, due to the equipartition theorem, comprises one third of the total thermal kinetic energy, the particles' nonrelativistic thermal momentum in the direction of the measured current will be given by

$$p_x^{\text{th}} = \sqrt{m_p k_B T_0}. \quad (4)$$

We fix the particles' initial temperature such that their kinetic energy is $k_B T_0 = 10^{-2} m_e c^2$. Thus, the protons' momentum along the current direction due to their initial thermal motion is given by

$$p_x^{\text{th}} = \frac{c}{10} \sqrt{m_p m_e}. \quad (5)$$

The total current density caused by the thermal noise will then be

$$j_{\text{th}} = \frac{p_x^{\text{th}} N_0}{m_p c \Delta z}, \quad (6)$$

where N_0 is the number of all particles in the simulation box and Δz the box's extent in the perpendicular direction not resolved in the simulation. Given that up to the particle number all the above quantities are fixed in our simulations, we can provide an engineering formula for the thermal current in our simulations

$$j_{\text{th}} = \frac{1}{10} \sqrt{\frac{m_e}{m_p}} \frac{N_0}{\Delta z} \approx 2 \times 10^{-3} \frac{N_0}{\Delta z}. \quad (7)$$

In all comparisons to numerical results we indicate this thermal noise level as a lower boundary below which the simulations' results need to be interpreted with great care. On the other hand, other effects due to the prepulse such as hydrodynamic expansion or pushing of the target's front are neglected, indicating that further disturbance of the simulation results may take place.

2.5 Acceleration by Coulomb explosion

2.5.1 Governing model

The basic concept of laser-ion acceleration via Coulomb explosion relies on the Coulomb repulsion of residual ions, collectively stripped of a large portion of the corresponding electrons. As a specific example of this basic ion acceleration concept we are going to study a refined, double-layered setup of a purely Coulomb explosion target [23]: it was proposed to mount a thin layer of light ions, protons in this case, of thickness $d_{CE,1}$ on a layer of heavier ones of thickness d_{CE} . Once a laser pulse has ionized both layers and ejected all electrons, the heavier ions are going to stay in place, while the lighter ones are repelled by the Coulomb force onward, resulting ideally in a collimated, dense bunch of light ions. In order to estimate the scheme's efficiency, we have to find a reasonable assumption on the ratio of electrons expelled from the target by the laser pulse. As a strongly simplifying assumption we assume the target to be ionized only by the prepulse. Neglecting any shielding of the ions' charge as well as the proton layer, the ratio of electrons expelled from the layer of heavy ions can be roughly approximated as the ratio of the laser pulse's total energy $\varepsilon_0 = P_0\tau_0$ to the total number of electrons in the target $N_{CE} = n_0d_{CE}\pi w_0^2$ and the energy required to remove one single electron from the heavy ion cloud $\Delta\varepsilon$. To estimate latter we employ the common assumption of the ions' potential to be one-dimensional up to a distance from the target of its transverse dimension $r_0 = 2w_0$. The binding energy of an electron to the cloud of heavy ions then becomes $\Delta\varepsilon = 2\pi e^2 n_0 d_{CE} r_0$ and we find the ratio of electrons expelled from the heavy ion layer to be

$$\nu_{CE} = \frac{\varepsilon_0}{\Delta\varepsilon N_{CE}}. \quad (8)$$

In the case $\varepsilon_0 > \Delta\varepsilon N_{CE}$ we assume all the electrons to be expelled from the heavy ion layer. In the assumed one-dimensional geometry the electric field exerted by the remaining layer of heavy ions will then be [23]

$$E_{CE} = 2\pi\nu_{CE}n_0Zed_{CE}, \quad (9)$$

where Z is the heavy ions' ionization level. One can then estimate that the light protons will be accelerated to energies of the order

$$\varepsilon_{CE} = m_p c^2 + eE_{CE}r_0,$$

where r_0 again is the acceleration length over which the one-dimensional approximation is assumed to hold. The proton current density is then given by

$$j_{CE} = \frac{p_{CE}}{m_p} \frac{N_{CE}}{w_0} \frac{d_{CE,1}}{d_{CE}}, \quad (10)$$

where the proton momentum is given by $p_{CE} = \sqrt{\varepsilon_{CE}^2/c^2 - m_p^2 c^2}$ and the additional factor $d_{CE,1}/d_{CE}$ results from the proton layer being thinner than the layer of heavy ions.

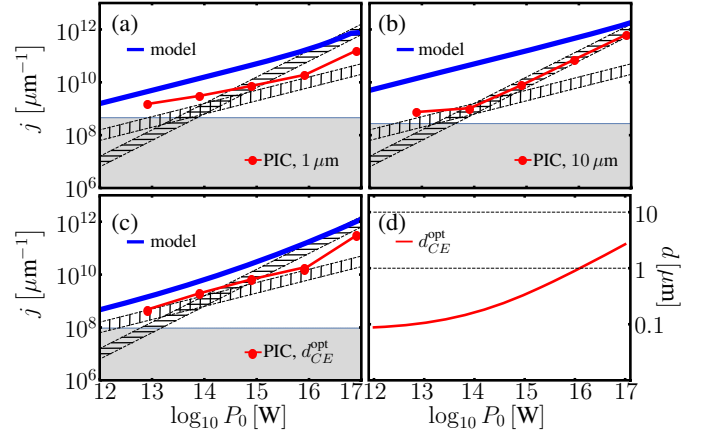


Fig. 2. Comparison of the proton currents resulting from three different target thicknesses in a Coulomb explosion setup for (a) $d_{CE} = 1 \mu\text{m}$, (b) $d_{CE} = 10 \mu\text{m}$ and (c) $d_{CE} = d_{CE}^{\text{opt}}$ and a lower cutoff energy of $\varepsilon_{\text{cut}} = 5 \text{ MeV}$ as compared to the theoretical model and (d) the dependence of the optimal target thickness on the laser power. For comparison ((a)–(c)): linear scaling (horizontal stripes) and square root scaling (vertical stripes) with the laser power. Gray shaded area: numerical sensitivity limit due to assumed thermal noise.

In order to provide an intuitive access to the proton currents to be expected according to the above theory, we derive a simple scaling law. Assuming the ratio of electrons expelled from the heavy ion layer does not saturate for the considered laser powers (as we confirmed numerically) we find the scaling $E_{CE} \sim \nu_{CE} \sim P_0$. The momentum of a proton accelerated in a Coulomb explosion setup can thus be estimated to be $p_{CE} = m_p c \sqrt{(\varepsilon_{CE}/m_p c^2)^2 - 1} \sim m_p \sqrt{E_{CE}/m_p} \sim P_0^{1/2}$, where $eE_{CE}r_0 \ll m_p c^2$ was used, as it holds for all studied laser powers. The resulting proton current density is then estimated to scale as

$$j_{CE} \sim p_{CE} d_{CE,1} \sim \begin{cases} \sqrt{P_0} & \text{fixed } d_{CE,1} \\ P_0 & d_{CE,1}^{\text{opt}} \sim \sqrt{P_0}. \end{cases} \quad (11)$$

Finally, in order to run the Coulomb explosion mechanism optimally, it was found from simulations that the heavy ion layer should have an optimum thickness of [24]

$$d_{CE}^{\text{opt}} = (0.4a_0 + 3) \frac{n_{cr}}{n_0} \lambda_0. \quad (12)$$

2.5.2 Comparison with 2D PIC modeling

We model the proposed double layer setup as consisting of a layer of protons mounted on a layer of heavy ions (s. Fig. 1a). Keeping in mind that the proposed double-layer setup needs to be manufactured, however, we relax the complication of a very thin target by assuming the proton layer to be only half as thick (in contrast to the thickness ratio 0.06 as employed in [23]) as the heavy ion layer, which for the optimal thickness already has to be sub- μm thin (s. Fig. 2d). For comparing the acceleration scheme's performance for various target geometries, we study three

different thicknesses of the heavy ion layer, namely the optimized, power-dependent thickness d_{CE}^{opt} and two fixed thicknesses of $1 \mu\text{m}$ or $10 \mu\text{m}$. The two fixed target thicknesses are chosen since d_{CE}^{opt} is always smaller than $10 \mu\text{m}$ but grows larger than $1 \mu\text{m}$ for laser powers above 10^{15} W (s. Fig. 2d).

We find that the exact solutions of equation (10) for the targets of fixed thicknesses $1 \mu\text{m}$ or $10 \mu\text{m}$ indeed predicts a scaling $j_{CE} \sim P_0^{1/2}$ (s. Figs. 2a and 2b), whereas for the target of optimal thickness d_{CE}^{opt} the current's scaling is predicted to shift from $j_{CE} \sim P_0^{1/2}$ to $j_{CE} \sim P_0$ (s. Fig. 2c) in the same manner as the optimal thickness shifts from a constant value to a scaling $d_{CE}^{opt} \sim P_0^{1/2}$ (s. Fig. 2d).

Apparently the theoretically predicted proton currents are not reached in the performed PIC simulations, indicating the model overestimates the proton current by almost one order of magnitude. We associate this stark discrepancy with the theoretically neglected return currents, neutralizing the remaining heavy ions' Coulomb field as well as with an overestimation of the electron expulsion efficiency. Nevertheless, the performed simulations should still reproduce the found scaling laws and general tendencies. In the numerical simulations, on the other hand, only the $1 \mu\text{m}$ - and the d_{CE}^{opt} -targets approximately satisfy the predicted scaling $j_{CE} \sim P_0^{1/2}$ for low laser powers (s. Figs. 2a and 2c). We note, however, that for the highest considered power $P_0 = 10^{17} \text{ W}$ in the numerical simulation we find a significant portion of the laser pulse to break through the targets of optimal thickness and $d_{CE} = 1 \mu\text{m}$. Thus, the studied Coulomb explosion mechanism develops a substantial similarity to a light sail mechanism and the related data point exhibits a considerably higher proton current than one would expect from extrapolating the low-power scaling behavior (s. Figs. 2a and 2c). The thicker target, on the other hand, exhibits a scaling $j_{CE} \sim P_0$ (s. Fig. 2b), which we attribute to a strong efficiency loss for lower laser powers since the electron return currents inside the thick target can efficiently compensate the heavy ions' Coulomb fields before a significant proton current can form. Due to this scaling of the proton current, the thickest target geometry produces a comparatively low overall current level for low laser powers, underrunning the predicted proton current by almost two orders of magnitude for $P_0 = 10^{14} \text{ W}$. The deviation from the linear scaling at a laser power $P_0 = 10^{13} \text{ W}$ seems to be attributable to thermal noise, whence we do not include this laser power in the refined interpretation and attribute in particular physical meaning to the $10 \mu\text{m}$ -target only down to a minimal laser power of $P_0 = 10^{14} \text{ W}$. We find the thickest target to produce the lowest proton current of all target geometries for this laser power (s. Fig. 2b). For laser powers $P_0 \leq 10^{15} \text{ W}$ we find the intermediate thickness $1 \mu\text{m}$ to produce the highest proton currents, indicating a delicate balance between large numbers of accelerated particles and high proton energies (s. Fig. 2a). For laser powers $P_0 \geq 10^{15} \text{ W}$ it seems that the target thickness, corresponding to the number of accelerated particles, dominates the proton current. This in-

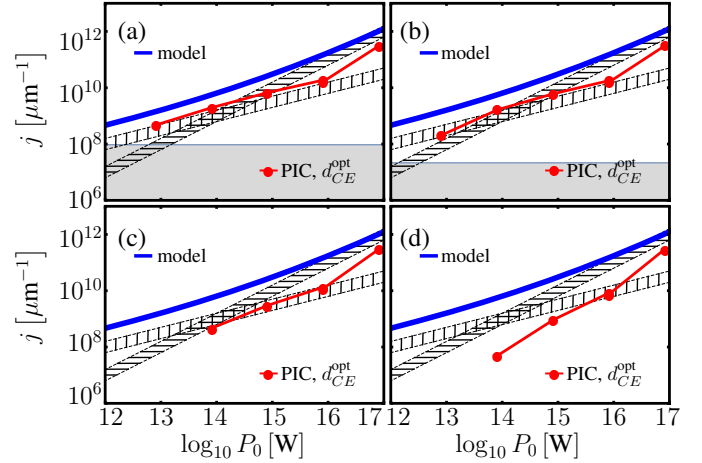


Fig. 3. Comparison of the proton current resulting from a Coulomb explosion setup as compared to the model for a lower cutoff energy of (a) 5 MeV, (b) 10 MeV, (c) 50 MeV and (d) 75 MeV. For comparison: linear scaling (horizontal stripes) and square root scaling (vertical stripes) with the laser power. Gray shaded area: numerical sensitivity limit due to assumed thermal noise.

dicates that all target geometries produce comparable proton energies, with the apparent differences in the currents being attributable to different numbers of accelerated particles and that for the thickest target at low laser powers there is a strong thermal contribution to a Coulomb explosion ion acceleration setup. This also explains the deviation from the linear scaling law with the laser power. Nevertheless, we find all target geometries to yield significantly lower currents than theoretically predicted, indicating an overall poor benchmarking performance of the employed theoretical model. Comparing the proton currents resulting from a target with optimal thickness at different lower cutoff energies, we find the simulated currents to differ only slightly when including protons up to a lower energy cutoff of $\varepsilon_{cut} = 10 \text{ MeV}$ only for laser powers to $P_0 \geq 10^{14} \text{ W}$. For $\varepsilon_{cut} = 50 \text{ MeV}$ we find the proton currents to be largely unaffected for laser powers $P_0 \geq 10^{15} \text{ W}$, while for $\varepsilon_{cut} = 75 \text{ MeV}$ only laser powers $P_0 \geq 10^{16} \text{ W}$ produce a current unaffected by changing ε_{cut} . We can thus conclude that the given laser powers produce mainly protons with more than the associated energies while the predicted scaling $j_{CE} \sim P_0$ is well reproduced, albeit at much smaller absolute currents (s. Fig. 3).

2.6 Acceleration by hole boring

2.6.1 Governing model

Unlike the previously discussed Coulomb explosion regime, hole boring denotes a radiation pressure acceleration in an overdense, thick target. The acceleration mechanism relies on the laser pulse piling up a thin electron spike, pushed forward by the ponderomotive force at the so-called piston velocity $v_{piston} = c\varepsilon/(1 + \varepsilon)$, where the parameter $\varepsilon = \sqrt{I/(m_p n_0 c^3)}$ [29] is introduced.

The resulting charge separation field pulls the ions behind, forming an electrostatic shock propagating through the target. We adopt a well-known analytical model predicting an ion velocity [29]

$$v_{\text{HB}} = \frac{2v_{\text{piston}}}{1 + \left(\frac{v_{\text{piston}}}{c}\right)^2}. \quad (13)$$

The resulting proton momentum is then given by

$$p_{\text{HB}} = m_p c \frac{2\varepsilon(1 + \varepsilon)}{1 + 2\varepsilon}. \quad (14)$$

Consequently, the proton current density is given by

$$j_{\text{HB}} = \frac{p_{\text{HB}}}{m_p} \frac{N_{\text{HB}}}{w_0}. \quad (15)$$

In order to estimate the number of protons accelerated in the studied hole boring scheme, it is advantageous to note that the propagation speed of the shock front is given by $v_{\text{HB}} = c\varepsilon/(1 + \varepsilon)$. The time over which the laser pulse will be acting on the shock front can be approximated in the laboratory frame to be given by $t_{\text{HB}} = \tau_0/(1 - v_{\text{HB}}/c)$. Approximating then the number of protons piled up in a hole boring setup after t_{HB} by the total number of protons in the volume the shock front traversed, i.e., assuming perfect ionization and capture of the protons by the shock front, we find

$$N_{\text{HB}} = n_0 v_{\text{HB}} t_{\text{HB}} \pi w_0^2. \quad (16)$$

Naturally, $N_{\text{HB}} < N_{\text{HB}}^{\text{max}} = n_0 d_{\text{HB}} \pi w_0^2$ has to always hold since the laser pulse cannot pile up more protons than are contained in its path through the whole thickness of the target. Thus, for a target that is too thin or an acceleration time which is too long, such that $d_{\text{HB}} < v_{\text{HB}} t_{\text{HB}}$, the number of protons accelerated in hole boring is $N_{\text{HB}}^{\text{max}}$.

Finally, we provide an approximate scaling law for the proton current also for hole boring. For all studied laser powers it holds $\varepsilon \ll 1$ and from this parameter's definition one concludes $\varepsilon \sim P_0^{1/2}$. Thus we conclude $v_{\text{HB}} \sim p_{\text{HB}} \sim P_0^{1/2}$. The proton current density resulting from a hole boring setup thus is expected to scale as

$$j_{\text{HB}} \sim p_{\text{HB}} N_{\text{HB}} \sim p_{\text{HB}} v_{\text{HB}} \sim P_0. \quad (17)$$

2.6.2 Comparison with 2D PIC modeling

Due to the conceptual simplicity of hole boring it is sufficient to only study one target geometry. We model a proton and electron layer three times thicker than one which allows for the onset relativistic transparency (Fig. 1b). In this way it is ensured that the laser pulse does not break through the target and the HB regime is maintained over the whole acceleration process. Also, varying the target thickness was found to have no effect on the proton current. As apparent from the theoretical considerations presented above, we assumed a full ionization of the target as

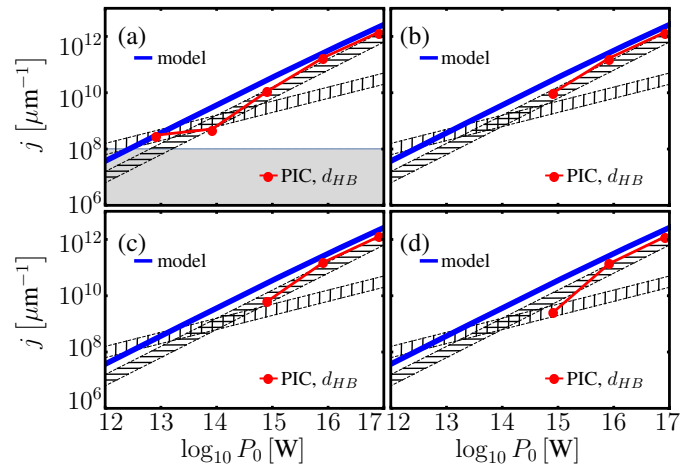


Fig. 4. Comparison of the proton current resulting from a hole boring setup as compared to the model for a lower cutoff energy of (a) 5 MeV, (b) 10 MeV, (c) 50 MeV and (d) 75 MeV. For comparison: linear scaling (horizontal stripes) and square root scaling (vertical stripes) with the laser power. Gray shaded area: numerical sensitivity limit due to assumed thermal noise.

well as the accelerated current to be formed by all protons in the laser pulse's path. From the good agreement between the presented theory and PIC simulations accounting for all protons above a lower cutoff energy of 5 MeV (s. Fig. 4a) we conclude the former assumption to be reasonable and the presented theory to describe the physical acceleration process satisfactorily. Furthermore, we find the predicted linear scaling with the laser power to be very well reproduced and even slightly overrun. Only at the lowest considered laser power $P_0 = 10^{13}$ W the PIC simulation deviates from a linear scaling, which we attribute to the thermal noise level. From comparing the proton currents at various lower cutoff energies, where the absence of a data point indicates that at the given laser power there is no current of protons above the chosen cutoff energy formed (s. Figs. 4b–4d), we infer that at low laser powers hole boring yields a current of a large number of rather low-energetic particles. At large laser powers, however, hole boring reliably produces a large number of high energy protons, as we infer from the fact that the proton current at laser powers $P_0 \geq 10^{15}$ W do not significantly differ for a lower cutoff energy of 50 MeV (s. Fig. 4c) or 75 MeV (s. Fig. 4d).

2.7 Light sail acceleration

2.7.1 Governing model

Just like hole boring, the laser piston, or light sail, regime relies on directly employing the longitudinal radiation pressure for ion acceleration. We adopt the theoretical description of [30] which is somewhat more involved than the previously studied static acceleration mechanisms of Coulomb explosion and hole boring. The proton dynamics in a light sail regime are governed by the set of coupled

differential equations [3,4]

$$\begin{aligned} \frac{dp}{dt} &= R(p) \frac{E_0^2(t-x/c)}{2\pi n_0 d_{LS}} \frac{\sqrt{p^2 + m_p^2 c^2} - p}{\sqrt{p^2 + m_p^2 c^2} + p} \\ p &= m_p v \sqrt{\frac{1}{1 - \left(\frac{v}{c}\right)^2}} \\ \frac{dx}{dt} &= v. \end{aligned} \quad (18)$$

The momentum dependent reflectivity is given by [60]

$$R(p) = \begin{cases} \frac{\pi \sigma^2(p)}{1 + (\pi \sigma(p))^2} & \text{if } a_0 < \sqrt{1 + \pi^2 \sigma^2(p)}, \\ \frac{(\pi \sigma(p))^2}{1 + a_0^2} & \text{if } a_0 > \sqrt{1 + \pi^2 \sigma^2(p)}, \end{cases} \quad (19)$$

where the boosted areal density of the light sail in the comoving reference frame is given by $\sigma(p) = \sigma_0 \lambda(p) / \lambda_0$, with the momentum dependent wavelength in the light sail's moving frame $\lambda(p)$ and the dimensionless areal density in the laboratory frame $\sigma_0 = n_0 d_{LS} / n_{cr} \lambda_0$. It was shown, that in an ideal light sail configuration with constant reflectivity $R \equiv 1$ and constant laser field strength $E_0 = \text{const.}$, a proton sheath acquires a momentum [30]

$$p_{LS} = m_p c \left(\sinh(u_{LS}) - \frac{\text{csch}(u_{LS})}{4} \right), \quad (20)$$

where we use $u_{LS} = \text{asinh}(\Omega_{LS} t_{LS} + h_{LS}^{3/2} + 3/2 h_{LS}) / 3$, $\Omega_{LS} = (3E_0^2) / (2\pi n_0 d_{LS} m_p c)$ and $h_{LS} = p_{LS,0} / m_p c + \sqrt{1 + p_{LS,0}^2 / m_p^2 c^2}$. The time over which the light sail acceleration is expected to be maintained was estimated to be $t_{LS} = 2\tau_0 (\varepsilon_0 / (n_0 \pi w_0^2 d_{LS} m_p c^2))^2 / 3$ [30]. Naturally, τ_0 is a lower limit for t_{LS} , so for $(\varepsilon_0 / (n_0 \pi w_0^2 d_{LS} m_p c^2))^2 < 3/2$ we set $t_{LS} = \tau_0$. As we will see later, the differences in final light sail momenta between the exact and the approximate theory are marginal for larger laser powers, proving approximating the laser pulse to be of constant amplitude and the light sail perfectly reflecting to be admissible in this parameter regime. The proton current density is then

$$j_{LS} = \frac{p_{LS}}{m_p} \frac{N_{LS}}{w_0}. \quad (21)$$

The number of protons accelerated in an ideal light sail setup is simply given by all particles contained in the sheath thickness $N_{LS} = d_{LS} n_0 \pi w_0^2$.

In order to run the light sail mechanism optimally, it was shown that the target should have a thickness, balancing between reflection of the laser pulse and a pre-mature break-through, due to the onset of relativistic transparency [4]. The optimum thickness was found to be given by [60]

$$d_{LS}^{\text{opt}} = \frac{a_0}{\pi} \frac{n_{cr}}{n_0} \lambda_0. \quad (22)$$

We finally estimate the scaling law for the proton current expected from a light sail setup. Inserting the definition of the parameters we derive for the optimal thickness d_{LS}^{opt} the following scaling $\Omega_{LS} t_{LS} \sim P_0^{3/2}$ for $(\varepsilon_0 / (n_0 \pi w_0^2 d_{LS} m_p c^2))^2 > 3/2$ and $\Omega_{LS} t_{LS} \sim P_0^{1/2}$ for $(\varepsilon_0 / (n_0 \pi w_0^2 d_{LS} m_p c^2))^2 < 3/2$, where we respected the varying scaling of t_{LS} . Furthermore, the balance condition $(\varepsilon_0 / (n_0 \pi w_0^2 d_{LS} m_p c^2))^2 = 3/2$ signifies the balance point $\Omega_{LS} t_{LS} \approx 1$, whence for $(\varepsilon_0 / (n_0 \pi w_0^2 d_{LS} m_p c^2))^2 < 3/2$ we can approximate $\sinh(u_{LS}) \sim \Omega_{LS} t_{LS}$ and for $(\varepsilon_0 / (n_0 \pi w_0^2 d_{LS} m_p c^2))^2 > 3/2$ we find $\sinh(u_{LS}) \sim (\Omega_{LS} t_{LS})^{1/3}$. In both cases the proton momentum thus scales as $p_{LS} \sim P_0^{1/2}$ and for the proton current density we expect a scaling

$$j_{LS} \sim p_{LS} d_{LS}^{\text{opt}} \sim P_0. \quad (23)$$

A similar argument shows that for a fixed target thickness one expects the same linear scaling.

2.7.2 Comparison with 2D PIC modeling

As a simple target is in principle required for light sail acceleration, we study a thin layer of protons and electrons (Fig. 1c). Analogous to the Coulomb explosion regime, in order to study the acceleration's efficiency for varying target geometries we investigate three different layer thicknesses, namely the optimized, power-dependent thickness d_{LS}^{opt} and two fixed thicknesses of 1 μm and 10 μm . The latter thickness violates the assumption $d_{LS} \ll \lambda_0$, underlying the derivation of equation (18). We study it as a limiting case and find that even in this case the agreement between theory and simulations is remarkable. We find the exact and approximate theoretical models introduced above to agree good within an order of magnitude (s. Figs. 5a–5c). The overestimation of the proton current by the approximate model at low laser powers is due to assuming a perfect reflectivity of the relativistic mirror, that is not yet fully achieved at the corresponding low radiation pressures. Also the PIC simulations follow the theoretical predictions in scaling as well to a very good extent, also in absolute numbers. There is, however, a slight deviation from the scaling $j_{LS} \sim P_0$ for the optimal thickness d_{LS}^{opt} (s. Fig. 5c). This behavior can most probably be attributed to imperfect proton capture due to the strong transversal ponderomotive force pushing the protons out of the interaction region and other onsetting plasma instabilities driven by high power lasers. A more discontinuous change in the scaling behavior is observed for the thin target $d_{LS} = 1 \mu\text{m}$ at the highest laser power $P_0 = 10^{17}$ W (s. Fig. 5a). This abrupt efficiency loss is due to the target's thickness falling below the optimal target thickness (s. Fig. 5d) and thus containing too few protons to follow the linear trend. A similar, particle number-dominated explanation most likely applies to the behavior of the over-thick light sail target $d_{LS} = 10 \mu\text{m}$ which maintains the linear scaling $d_{LS}^{\text{opt}} \sim P_0$ over all studied laser powers. Since the target, however, is always too thick to admit relativistic transparency and thus break-through of the laser pulse

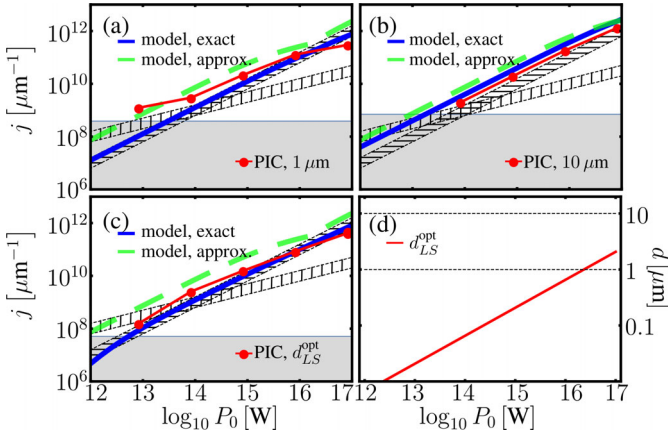


Fig. 5. Comparison of the proton currents resulting from a light sail setup for three different target thicknesses (a) $d_{LS} = 1 \mu\text{m}$, (b) $d_{LS} = 10 \mu\text{m}$ and (c) $d_{LS} = d_{LS}^{\text{opt}}$ as compared to the exact and approximate theoretical models. (d) Dependence of the optimal target thickness on the laser power. For comparison ((a)–(c)) linear scaling (horizontal stripes) and square root scaling (vertical stripes) with the laser power. Gray shaded area: numerical sensitivity limit due to assumed thermal noise.

through the target, this target rather operates in a hole-boring regime, as is also supported from the close similarity of the simulations results to those of hole boring (s. Fig. 4a). We also see that light sail operation at low laser powers below 10^{14} W requires sub- μm thin targets and thus ultra-high laser contrast. Furthermore, it shows that at a laser power $P_0 = 10^{13}$ W the $1 \mu\text{m}$ thin target yields larger proton currents than the target with optimal thickness (s. Fig. 5a), most likely because it yields larger particle numbers. The proton currents from the light sail target with $d_{LS} = 10 \mu\text{m}$ are not particularly discussed here, since they need to be interpreted with great care due to the hole boring mechanism that comes additionally into play. When considering only protons above an energy of 10 MeV the optimal thickness target then does not yield any proton current for $P_0 \leq 10^{14}$ W, demonstrating that a light sail at such low intensities produces merely thermal protons and is rather inefficient (s. Fig. 6b). For a laser powers $P_0 \geq 10^{14}$ W, on the other hand, the optimal-thickness target produces a current of particles almost exclusively at energies larger than 50 MeV (compare Figs. 6b and 6c). We thus conclude that a true light sail acceleration is efficiently operated only at larger laser powers. Lastly, at the largest laser power $P_0 = 10^{17}$ W we find the currents to be virtually independent of the lower cutoff-energy of even up to $\varepsilon_{\text{cut}} = 75$ MeV.

2.8 Target normal sheath acceleration

In addition, we consider a target design optimized for TNSA, in order to benchmark the high-energy schemes against the most conventional thermal acceleration scheme. To this end, we model a linearly polarized laser pulse to hit a typical TNSA target with thickness of $3 \mu\text{m}$ with a $0.2 \mu\text{m}$ thin hydrogen layer on the back

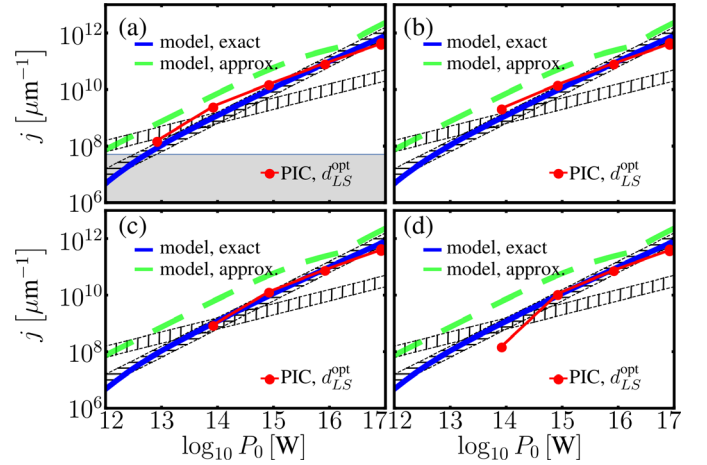


Fig. 6. Comparison of the proton current resulting from a light sail setup as compared to the models for a lower cutoff energy of (a) 5 MeV, (b) 10 MeV, (c) 50 MeV and (d) 75 MeV. For comparison: linear scaling (horizontal stripes) and square root scaling (vertical stripes) with the laser power. Gray shaded area: numerical sensitivity limit due to assumed thermal noise.

surface (s. Fig. 1d) under an incidence angle of $\pi/4$. We then compare the efficiency of the three mentioned high-intensity acceleration schemes to the performance of conventional TNSA.

2.8.1 Governing model

For the sake of simplicity, for modeling this acceleration mechanism we resort to the one-dimensional model of a heated plasma expanding into vacuum [37] along the x -direction with a velocity distribution $v_{\text{TNSA}} = c_s + x/t$ and a density profile $n = n_0 \exp[-(1+x/(c_s t))]$, where $c_s = \sqrt{(Zk_B T)/m_p}$ is the speed of sound, Z the ions' ionization level, k_B the Boltzmann constant and T the plasma temperature. The model is only defined for $x > x^{\text{min}}(t) = -c_s t$ and the front of the expanding ion cloud is located at $x^{\text{max}}(t) = (2 \log[\omega_{p,i} t] - 1)c_s t$. Consequently, the ion current density, given by the product of the transverse size of the acceleration region, approximated by w_0 with the spatial integral over the product of the particle density and the respective velocity through the plasma expansion volume, is given by

$$j_{\text{TNSA}} = n_0 w_0 \int_{x^{\text{min}}(t_{\text{TNSA}})}^{x^{\text{max}}(t_{\text{TNSA}})} dx \sqrt{\frac{v_{\text{TNSA}}^2}{1 - \left(\frac{v_{\text{TNSA}}}{c}\right)^2}} e^{-\left(1 + \frac{x}{r_{\text{TNSA}}}\right)}, \quad (24)$$

where we defined the distance a plasma perturbation travels during the operation time of TNSA $r_{\text{TNSA}} = c_s t_{\text{TNSA}}$ with $t_{\text{TNSA}} = 1.3\tau_0$ an effective estimate of how long the TNSA mechanism can be upheld and the additional square root factor is the position dependent Lorentz factor of the proton cloud. The proton plasma frequency is given by $\omega_{p,i} = \sqrt{(4\pi n_0 e^2)/m_p}$ and as an estimate for the plasma temperature we employ the ponderomotive model

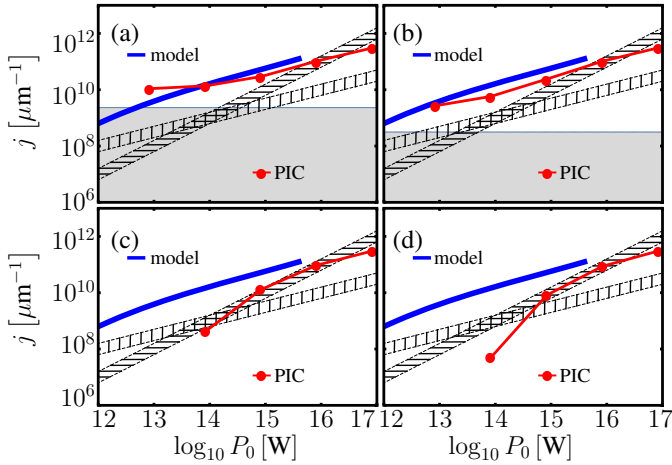


Fig. 7. Comparison of the proton current resulting from a TNSA setup as compared to the model for a lower cutoff energy of (a) 5 MeV, (b) 10 MeV, (c) 50 MeV and (d) 75 MeV. For comparison: linear scaling (horizontal stripes) and square root scaling (vertical stripes) with the laser power. Gray shaded area: numerical sensitivity limit due to assumed thermal noise.

$T = m_e \left(\sqrt{1 + a_0^2} - 1 \right)$. It is important to note, however, that the actual dependence of the electron temperature on the laser parameters can be more complex than this simple model [61]. This increased complexity, on the other hand, does not influence the predicted ion flux scalings significantly, whence we disregard it for the sake of a simple interpretability.

2.8.2 Comparison with 2D PIC modeling

As a benchmark TNSA target we consider a target of heavy ions with a thin proton layer on the backside (s. Fig. 1d). We find the resulting proton current to closely follow the theoretical predictions in absolute numbers, particularly confirming the expected scaling $j_{\text{TNSA}} \sim P_0^{1/2}$. Only the data point at $P_0 = 10^{13}$ W does not follow the theoretical prediction (s. Fig. 7a). Taking into account that the modeled curve falls below that thermal noise level at this laser power, the observed deviation from the analytical model is most probably due to thermal noise in the simulation. The otherwise good agreement between theory and numerical experiments, however, is by no means surprising, since TNSA has been studied abundantly and is theoretically well understood. Taking into account, on the other hand, that the simulated proton currents at higher lower cutoff energies fall significantly off even for high laser powers confirms that TNSA produces mostly low-energy protons (s. Figs. 7b–7d). These are accelerated, albeit, at a large number, yielding the resultant high proton currents.

2.9 Comparing high intensity acceleration schemes

Comparing the results from simulations of all the considered schemes (s. Fig. 8) one can draw several conclusions. The theoretical models (s. Fig. 8a) predict TNSA

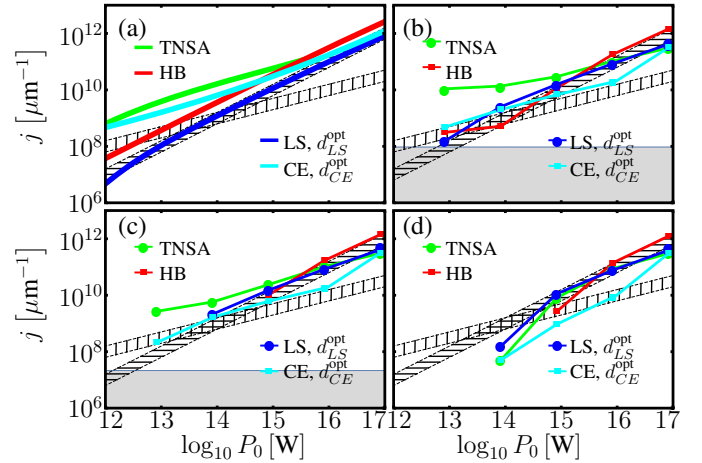


Fig. 8. (a) Comparison of the theoretically predicted proton currents resulting from all four studied acceleration setups. ((c)–(d)) Comparison of the simulated proton currents resulting from all four studied acceleration schemes for a lower cutoff energy of (b) 5 MeV, (c) 10 MeV and (d) 75 MeV. For comparison: linear scaling (horizontal stripes) and square root scaling (vertical stripes) with the laser power. Gray shaded area: numerical sensitivity limit due to assumed thermal noise.

to provide the largest proton currents for laser powers $P_0 \lesssim 10^{15}$ W while at larger powers hole boring provides larger currents, due to its favorable scaling with the laser power. The light sail mechanism is predicted to always yield smaller currents than hole boring, due to the smaller number of accelerated protons, but eventually surpasses the TNSA currents for $P_0 \gtrsim 10^{16}$ W.

The results of the performed two-dimensional PIC simulations largely confirm these predictions. In general, the simulated currents of all protons with energies above 5 MeV (s. Fig. 8b) is strongly reminiscent of the theoretical prediction (s. Fig. 8a). In particular, for laser powers $P_0 < 10^{15}$ W TNSA gives much larger currents than the other schemes, but the current is mostly formed by low-energy protons. When accounting only for protons with energy above 75 MeV, TNSA is less efficient than light sail and for small laser powers it is also less efficient than Coulomb explosion (s. Fig. 8d). This is due to the TNSA mechanism quickly establishing strong accelerating fields for a large number of particles. However, the acceleration is spatially confined to the vicinity of the interface between the vacuum and the thermally expanding plasma. The rapid expansion of plasma leads to a quick reduction of the number of protons that experience the accelerating field at this interface. Thus, the process favors acceleration of a large number of protons but to a limited energy. In comparison, Coulomb explosion and light sail provide a control of the number of accelerated protons by tuning the thickness of the target. Thus one can optimize the thickness so that the laser pulse energy is not entirely consumed for accelerating a large number of particles, but more directed towards the acceleration of high-energy protons. Furthermore, light sail is particularly designed for accelerating a limited number of particles to a high energy.

As one can see, for laser powers $P_0 \geq 10^{15}$ W the current is almost insensitive to introducing a lower proton energy threshold of up to 75 MeV (s. Figs. 8b–8d), indicating that almost all accelerated have larger energies.

At the range $P_0 < 10^{15}$ W hole boring is difficult to distinguish from TNSA, thus it has similar features, but is substantially less efficient than TNSA. On the other hand, for a laser power above order $P_0 \gtrsim 10^{15}$ W hole boring provides a significantly larger current than all other schemes (s. Figs. 8b–8d). This is explained by the fact that it can provide acceleration to a certain level of energy for a large number of protons. This number is proportional to the pulse energy, because the mechanism gives roughly the same acceleration for an increasing number of protons as the pulse penetrates through the target until it is depleted. Thus, if one aims at accelerating a large number of particles to a certain energy in the range of tens of MeV, hole boring seems to provide the optimal strategy for high pulse powers. The scaling law for the hole boring fits well the trend of $j_{\text{HB}} \sim P_0$. At high powers this establishes its dominance over the TNSA, which follows the trend of $P_0^{1/2}$.

The light sail mechanism is efficient in terms of delivering the laser power to a limited number of protons, giving them very high energy. In particular, when accounting for only the protons of above 75 MeV energy, it provides the best results for $P_0 = 10^{15}$ W (s. Fig. 8d). For larger laser powers, however, the proton current increases less favorably as compared to the hole boring regime, due to a slower rate of growth in the number of accelerated protons.

3 Discussion and outlook

The ion acceleration mechanisms studied in this work are likely to become the backbone of high-power laser ion acceleration. We have provided a systematic access to the opportunities posed by these mechanisms to be implemented at currently available as well as future facilities.

Aiming at providing a better understanding of their potential in the context of particular applications, we introduced the so-called effective current as a single parameter, quantifying both the number and energies of the accelerated ions. Thus, the effective current is a measure for a laser-ion accelerator's efficiency in transforming laser energy into accelerated ions. In order to obtain conclusions of general relevance we computed this parameter for various theoretical models of laser-ion acceleration. To identify the predictive power of the analytical results under realistic conditions we then benchmarked the theory against elaborate two-dimensional PIC simulations. Based on this benchmarking we could assess for which laser powers and required minimal ion energies the employed analytical models describe the physics of laser-ion acceleration reasonably well and for which parameters they need to be interpreted with care (s. Fig. 9).

Benchmarking the studied high-power acceleration schemes to the broadly employed TNSA scheme we revealed several promising behaviors and identified their

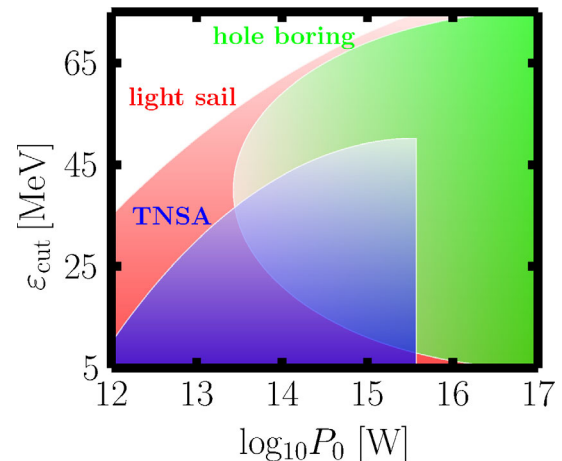


Fig. 9. Overview over regions of laser power P_0 and minimal required ion energy ε_{cut} where the benchmarked laser-ion acceleration models satisfactorily match the simulated proton currents. At low intensities where the thermal noise dominated the proton current its scaling was extrapolated. Coulomb explosion is excluded from the overview due to its overall low benchmarking performance.

strengths as well as weaknesses. We found that for laser powers above 1 PW essentially all studied high-power ion acceleration schemes surpass the ion currents of TNSA, especially when higher ion energies are required, as the latter's current is formed mostly by low-energy ions.

The results presented here can serve as a guidance for the design and planning of upcoming laser-ion acceleration facilities. Comparing the operation parameters of any high-power laser facility to those studied here will allow to assess the accessibility of all studied major laser-ion acceleration schemes as well as the ion currents to be reachable.

This research was supported by the Knut and Alice Wallenberg project PLIONA. The simulations were performed on resources provided by the Swedish National Infrastructure for Computing (SNIC) at PDC and HPC2N. Open access funding provided by Max Planck Society.

Author contribution statement

All the authors were involved in the preparation of the manuscript. All the authors have read and approved the final manuscript.

Open Access This is an open access article distributed under the terms of the Creative Commons Attribution License (<http://creativecommons.org/licenses/by/4.0>), which permits unrestricted use, distribution, and reproduction in any medium, provided the original work is properly cited.

References

1. M. Borghesi et al., Fusion Sci. Technol. **49**, 412 (2006)
2. S.S. Bulanov et al., Med. Phys. **35**, 1770 (2008)

3. H. Daido, M. Nishiuchi, A.S. Pirozhkov, Rep. Prog. Phys. **75**, 056401 (2012)
4. A. Macchi, M. Borghesi, M. Passoni, Rev. Mod. Phys. **85**, 751 (2013)
5. S.P. Hatchett et al., Phys. Plasmas **7**, 2076 (2000)
6. S.C. Wilks et al., Phys. Plasmas **8**, 542 (2001)
7. M. Roth et al., Phys. Rev. Spec. Top. Accel. Beams **5**, 061301 (2002)
8. A.J. Mackinnon et al., Phys. Rev. Lett. **88**, 215006 (2002)
9. T.E. Cowan et al., Phys. Rev. Lett. **92**, 204801 (2004)
10. M. Passoni, L. Bertagna, A. Zani, New J. Phys. **12**, 045012 (2010)
11. T. Tajima, D. Habs, X. Yan, in *Reviews of Accelerator Science and Technology* (2009), Vol. 2, p. 201
12. L. Robson et al., Nat. Phys. **3**, 58 (2007)
13. I.J. Kim et al., Phys. Rev. Lett. **111**, 165003 (2013)
14. K.A. Flippo et al., Phys. Plasmas **15**, 056709 (2008)
15. S. Buffechoux et al., Phys. Rev. Lett. **105**, 015005 (2010)
16. M. Burza et al., New J. Phys. **13**, 013030 (2011)
17. S.A. Gaillard et al., Phys. Plasmas **18**, 056710 (2011)
18. K. Markey et al., Phys. Rev. Lett. **105**, 195008 (2010)
19. S.M. Pfotenhauer et al., New J. Phys. **12**, 103009 (2010)
20. T. Ditmire et al., Nature **386**, 54 (1997)
21. V.F. Kovalev, V.Y. Bychenkov, K. Mima, Phys. Plasmas **14**, 103110 (2007)
22. V.F. Kovalev et al., Phys. Plasmas **14**, 053103 (2007)
23. T. Esirkepov et al., Phys. Rev. Lett. **89**, 175003 (2002)
24. T. Esirkepov, M. Yamagiwa, T. Tajima, Phys. Rev. Lett. **96**, 105001 (2006)
25. A.V. Korzhimanov, A.A. Gonoskov, A.V. Kim, A.M. Sergeev, J. Exp. Theor. Phys. Lett. **86**, 577 (2007)
26. S.S. Bulanov et al., Phys. Rev. E **78**, 026412 (2008)
27. L.O. Silva et al., Phys. Rev. Lett. **92**, 015002 (2004)
28. D. Haberberger et al., Nat. Phys. **8**, 95 (2012)
29. T. Schlegel et al., Phys. Plasmas **16**, 083103 (2009)
30. T. Esirkepov et al., Phys. Rev. Lett. **92**, 175003 (2004)
31. S.V. Bulanov et al., Phys. Rev. Lett. **104**, 135003 (2010)
32. A. Henig et al., Phys. Rev. Lett. **103**, 245003 (2009)
33. S. Kar et al., Phys. Rev. Lett. **109**, 185006 (2012)
34. A.A. Gonoskov, A.V. Korzhimanov, V.I. Eremin, A.V. Kim, A.M. Sergeev, Phys. Rev. Lett. **102**, 184801 (2009)
35. F. Mackenroth, A. Gonoskov, M. Marklund, Phys. Rev. Lett. **117**, 104801 (2016)
36. Z. Major et al., Rev. Las. Eng. **37**, 431 (2009)
37. P. Mora, Phys. Rev. Lett. **90**, 185002 (2003)
38. P. Mora, Phys. Rev. E **72**, 056401 (2005)
39. M. Nishiuchi et al., Phys. Lett. A **357**, 339 (2006)
40. M. Lontano, M. Passoni, Phys. Plasmas **13**, 042102 (2006)
41. J. Schreiber et al., Phys. Rev. Lett. **97**, 045005 (2006)
42. A.V. Gurevich, L.V. Pariiskaya, L.P. Pitaevskii, Sov. Phys. J. Exp. Theor. Phys. **36**, 274 (1972)
43. J.E. Crow, P.L. Auer, J.E. Allen, J. Plasma Phys. **14**, 65 (1975)
44. A.V. Gurevich, A.P. Meshcherkin, Sov. Phys. J. Exp. Theor. Phys. **53**, 937 (1981)
45. D.S. Dorozhkina, V.E. Semenov, Phys. Rev. Lett. **81**, 2691 (1998)
46. V.F. Kovalev, V.Yu. Bychenkov, Phys. Rev. Lett. **90**, 185004 (2003)
47. S.S. Bulanov et al., Phys. Plasmas **23**, 056703 (2016)
48. L. Yin et al., Las. Part. Beams **24**, 291 (2006)
49. B. Qiao et al., Phys. Rev. Lett. **102**, 145002 (2009)
50. W. Yu et al., Phys. Rev. E **72**, 046401 (2005)
51. B. Hegelich et al., Nature **439**, 441 (2006)
52. C.A.J. Palmer et al., Phys. Rev. Lett. **106**, 014801 (2011)
53. L. Ji, A. Pukhov, B. Shen, New J. Phys. **16**, 063047 (2014)
54. M. Chen et al., Phys. Rev. Lett. **103**, 024801 (2009)
55. S. Bastrakov et al., J. Comput. Sci. **3**, 474 (2012)
56. J.B. Kim, S. Göde, S.H. Glenzer, Rev. Sci. Instrum. **87**, 11E328 (2016)
57. M. Gauthier et al., Rev. Sci. Instrum. **87**, 11D827 (2016)
58. I. Prencipe et al., Plasma Phys. Control. Fusion **58**, 034019 (2016)
59. T.Zh. Esirkepov et al., Nucl. Instrum Methods Phys. Res. A **745**, 150 (2014)
60. A. Macchi, S. Veghini, F. Pegoraro, Phys. Rev. Lett. **103**, 085003 (2009)
61. A. Yogo et al., Sci. Rep. **7**, 42451 (2017)